A EUROPEAN JOURNAL

CHEMPHYSCHEM

OF CHEMICAL PHYSICS AND PHYSICAL CHEMISTRY

Accepted Article

Title: Ab Initio Cyclic Voltammetry onCu(111), Cu(100) and Cu(110) in Acidic, Neutral and Alkaline Solutions

Authors: Alexander Bagger, Rosa M. Arán-Ais, Joakim Halldin Stenlid, Egon Campos dos Santos, Logi Arnarson, Kim Degn Jensen, Maria Escudero Escribano, Beatriz Roldan Cuyena, and Jan Rossmeisl

To be cited as: *ChemPhysChem* 10.1002/cphc.201900509

Link to VoR: http://dx.doi.org/10.1002/cphc.201900509

A Journal of

ChemPubSoc Europe

WILEY-VCH

www.chemphyschem.org

Ab Initio Cyclic Voltammetry on Cu(111), Cu(100) and Cu(110) in Acidic, Neutral and Alkaline Solutions

PhD Alexander Bagger[*],
PhD Rosa M. Arán-Ais [†],
PhD Joakim Halldin Stenlid[‡],
Egon Campos dos Santos[§],
PhD Logi Arnarson[*],
PhD Kim Degn Jensen[*],
Assistant Professor María Escudero-Escribano[*],
Professor Beatriz Roldan Cuenya[†],
Professor Jan Rossmeisl[*¶]

August 20, 2019

[*]Department of Chemistry, University of Copenhagen, Universitetsparken 5, Copenhagen, Denmark
[†]Department of Interface Science, Fritz Haber Institute of the Max Planck Society, 14195 Berlin, Germany
[‡]Department of Physics, Stockholm University, SE-106 91 Stockholm, Sweden
[§]Departamento de Quimica, ICEx, Universidade Federal de Minas Gerais, Belo Horizonte, 31.270-901, Minas Gerais, Brazil
[¶]corresponding author: jan.rossmeisl@chem.ku.dk

Abstract

Electrochemical reactions depend on the electrochemical interface between the electrode surfaces and the electrolytes. To control and advance electrochemical reactions there is a need to develop realistic simulation models of the electrochemical interface to understand the interface from an atomistic point-of-view. Here we present a method for obtaining thermodynamic realistic interface structures, a procedure we use to derive specific coverages and to obtain *ab initio* simulated cyclic voltammograms. As a case study, the method and procedure is applied in a matrix study of three Cu facets in three different electrolytes. The results have been validated by direct comparison to experimental cyclic voltammograms. The alkaline (NaOH) cyclic voltammograms are described by H^* and OH^*, while in neutral medium ($KHCO_3$) the CO_3^* species are dominating and in acidic (KCl) the Cl^* species prevail. An almost one-to-one mapping is observed from simulation to experiments giving an atomistic understanding of the interface structure of the Cu facets. Atomistic understanding of the interface at relevant eletrolyte conditions will further allow realistic modelling of electrochemical reactions of importance for future eletrocatalytic studies.

Introduction

Electrochemical energy conversion technologies are key in the transition to a sustainable society[1]. Despite the long and well-established history of (electro)catalysis, further understanding of the electrocatalytic interface for electrochemical reactions is needed. Computational studies within catalysis have e.g. revealed scaling relations[2, 3], which have been used to gain fundamental insight of catalytic reactions. This has in combination with computational screening for active surfaces[4] accelerated catalyst development, as the scaling relations can be used to derive *Sabatier* principles between calculated binding energies and the experimental activities of materials for key reactions[5, 6]. However, in these models, inclusion of the electrolyte or the surrounding conditions have only been sparsely investigated at the atomic-scale, but interest has increased in the recent years[7].

A particular useful experimental technique to gain an understanding of the catalyst-electrolyte interface is cyclic voltammograms (CVs). CVs can be carried out on different electrode materials. However, for the purpose of gaining atomistic insight it is preferable on well characterized single crystal electrodes. Distinct oxidation and reduction features can be observed in the CVs, which define the electrochemical properties of the electrochemical interface. Under specific experimental conditions (pH, anions, cations, scan rate, *etc.*) the features observed in the CVs can be considered a fingerprint of the changes in the interface structure. Ultimately, explaining the features observed in a CV gives a deep understanding of the complex electrochemical interface region.

To date, one of the most intensively studied single crystal system is Pt[8, 9, 10, 11, 12], as Pt materials are state-of-the-art catalysts in e.g. polymer electrolyte membrane fuel cells. Other metallic single crystal surfaces such as Ag[13, 14], Au[8, 9], Pd[15, 10], Rh[10], Ir[8, 16], Ru[17] and Cu[18, 19, 20, 21, 22, 23] have also been electrochemical investigated in the literature.

Cu single crystals are an interesting electrochemical interface to study as Cu metal has been shown to enable electrochemical CO_2 and CO reduction reactions towards valuable hydrocarbon and alcohol products[24, 25, 26, 27] and moreover the product distribution have been shown to be dependent on both the different facets and the compositions of the electrolyte [28, 29, 30, 31, 32]. Hence, understanding Cu single crystals with different electrolyte conditions in the metallic phase is of great interest.

In Figure 1**a**, the *Pourbaix* diagram for Cu shows stable phases under aqueous conditions as a function of the Standard Hydrogen Electrode (SHE) potential and pH, and the dashed black line indicate the potential versus the reversible hydrogen electrode (V_{RHE}). In this work, only the potentials and pH values where metallic Cu is stable is of interest, as this is where the electrochemical CO_2 and CO reduction reactions takes place. Figure 1**a** have been colored denoting the three pH-potential regions in which the electrochemical interface will be screened, corresponding to the following electrolyte

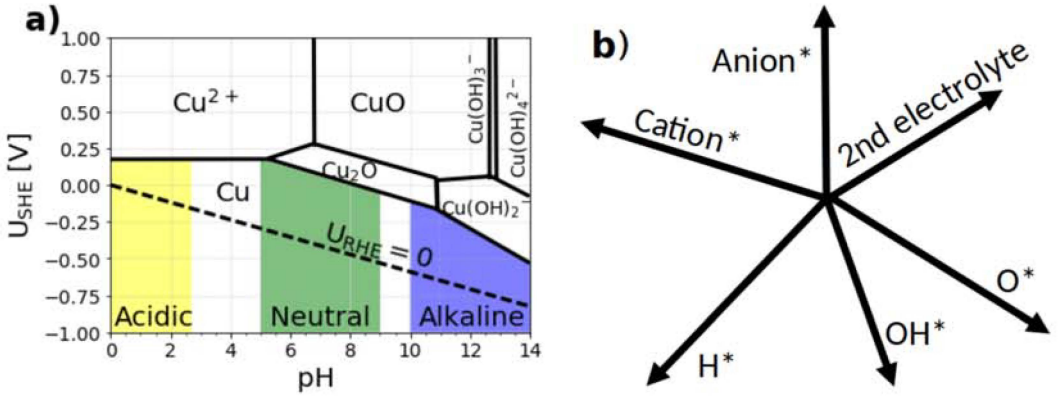

Figure 1: (a) Pourbaix diagram of Cu shwoing the stable phases as a function of potential (U_{SHE}) and pH at 25°C and the dashed line indicate U_{RHE}=0 V. Data is adapted from[37]. (b) Schematic of the electrolyte parameter space when investigating electrolytes in contact with a metal facet. The 2nd electrolyte corresponds to mixing multiple anions and cations.

conditions; Acidic (yellow), Neutral (green) and Alkaline (blue).

Metallic Cu single crystals have been previously investigated experimentally. For instance, Cu(111) in alkaline NaOH conditions has been studied by CV showing asymmetric double adsorption peaks around 0.05 V_{RHE} and double desorption peaks around -0.05 V_{RHE}.[21, 19, 18, 20] For Cu(100) in NaOH, CVs have been found stable with symmetric adsorption and desorption peaks observed around -0.15 V_{RHE}.[19, 18, 20] However, as recently shown in a comprehensive work and literature study by *Engstfeld et. al*[23], the Cu(100) CV peak shape, size and potential depends on both, preparation procedure and amount of residual O_2 in the electrolyte. Clearly, this introduces several uncertainties for the interpretation of the Cu CVs. For Cu(110) in NaOH, a relatively flat CV has been observed.[20]

In the intermediate (neutral) pH range, single crystal CVs on Cu(111) and Cu(100) have been measured in a CO(g) saturated phosphate buffer.[32] These experiments show adsorption and desorption peaks for Cu(100) around -0.3 V_{RHE}, in good agreement with our recent calculations on Cu(100) with CO and phosphate species[29].

In the acidic region, CVs have been measured for Cu(111), Cu(100) and Cu(110) in $HClO_4$, showing featureless (flat) CVs.[22] Below the typical CV potential region of Cu, in the HER region, reconstruction of the Cu(100) facet has been observed by STM.[33] Adding HCl to the $HClO_4$ electrolyte or using HCl electrolyte changes the Cu(111) and Cu(100) CV from featureless to having broad adsorption and desorption features at low potentials.[34, 35, 36]

Herein we study the Cu(111), Cu(100) and Cu(110) facets by *Ab Initio* Molecular Dynamics (AIMD)[38, 39] simulations of explicit electrolytes in contact with the surfaces. From these, we obtain

energetics as a function of the workfunction. This can be linked to the potential and ionic strength dependence by employing the Generalized Computational Hydrogen Electrode (GCHE)[40, 41, 29], as a posterior analysis of the system. This scheme allows explicit calculation of interface phase diagrams, from which the coverage of species can be derived and allows to obtain theoretical CVs for a set of surface structures. The theoretical CVs are then compared directly to experimental CVs and, when features allow it, a simple fitting procedure from experiment to the calculated states were carried out. Where the fitting only adjusts the binding energies of the simulated states ($\Delta E_{H_{fit}} = \Delta E_{H_{sim}} + E_{fit}$). This means that structures not considered in the simulations, but existing in reality, cannot be fitted or considered states can be overfitted. Furthermore, It should be noted that computational CVs are a less studied field, due to the difficulties of simulating the electrochemical interface, as compared to binding energy and other reactivity trend studies. Whereas, calculation of adsorbate coverages can be found in the literature.[42, 43, 41, 44]

Investigating the three Cu facets with three pH/electrolyte regions entails a massive number of parameters to be simulated/screened. This parameter space is shown in Figure 1**b**, with coverages of H*, OH*, O*, Cation(s), Anion(s) and 2nd electrolyte parameters that in principle require explicit calculations as well as their combinations (2nd electrolyte refers to secondary electrolyte effects). For example, a first approach would be to only consider H* and OH* states and their combinations up to half a monolayer (ML) coverage in a 12 atom unit-cell, which requires 7×7 = 49 AIMD simulations. Hence, including Cation(s), Anion(s) and 2nd electrolyte will quickly become an unsumountable computational task to span the whole parameter space. As a consequence, one has to be selective with respect to resources and iteratively select relevant electrolyte parameters to simulate.

This work uses a method that gives an interface in equilibrium with the electrochemical conditions, which ideally, should correspond to the experimental CV profiles. However, the modelling does have its limitations and assumptions, which are listed below:

- No reconstruction of the Cu(*hkl*) facet is considered.
- The simulated CVs only includes structures/adsorbates which are selected with respect to the electrolyte (*i.e.* no impurities).
- The simulated CVs corresponds to a reversible CV scan. Here the comparison is carried out with respect to the anodic scans.
- The simulated CVs and available coverages are limited by the finite unit-cell size.
- Only some configurations (naturally occuring in the AIMD) are considered in the simulations.
- Estimating the adsorbates entropy in the interface with respect to the electrolyte is difficult.

Finally, it is important to realize that the peak positions of the simulated CV will rely on absolute calculated adsorption energies which are related to a larger error than trends in adsorption energies,

Table 1: Experimental and simulation matrix investigation of the three Cu facets in three different Ar saturated electrolyte and pH conditions. The top row for each entry shows the electrolyte conditions while the lower row shows the included simulated surface adsorbates.

	Acidic (pH∼1)	Neutral (pH∼8.3)	Alkaline (pH∼13)
Cu(111)	0.1M $HClO_4$ + 0.01M KCl	0.1M $KHCO_3$	0.1M NaOH
	H^*, OH^*, Cl^*	H^*, OH^*, HCO_3^*, CO_3^*	H^*, OH^*
Cu(100)	0.1M $HClO_4$ + 0.01M KCl	0.1M $KHCO_3$	0.1M NaOH
	H^*, OH^*, Cl^*	H^*, OH^*, HCO_3^*, CO_3^*	H^*, OH^*
Cu(110)	0.1M $HClO_4$ + 0.01M KCl	0.1M $KHCO_3$	0.1M NaOH
	H^*, OH^*, Cl^*	H^*, OH^*, HCO_3^*, CO_3^*	H^*, OH^*

which is typically the strength of the successful volcano and scaling relation based Density Functional Theory (DFT) studies[2, 3]. However, as we carry out an experimental and simulation type of matrix study between Cu facets and electrolytes shown in Table 1, this mapping allows us to cross-reference our absolute values and hence make our conclusions more robust.

Methodology and Results

The procedure to make *ab initio* cyclic voltammograms is explained here and is followed by simulations, fits and experiments of Cu(*hkl*) crystals in alkaline, neutral and acid media. Figure 2 summarizes the five steps used to generate the simulated CVs which are:

(1) Relevant simulations of electrolyte structures are performed. For aqueous electrolytes this comprises the clean water-covered surface, H^*, OH^*, potentially also O^*, cations, anions and other electrolyte species/intermediates.

(2) The chemical potential is set for all species with respect to electrolyte conditions, accounting for pH, electrode potential and concentrations (see equation (1)).

(3) *Boltzmann* weighting is carried out to give a distribution with the most stable configurations at different potentials (see equation (2)).

(4) The slope of the Boltzmann-weighted energy corresponds to the charge of the interface. Differentiating the Boltzmann weighted energetics, one obtains the isotherm from the surface.

(5) Differentiating one more time and multiplying with a chosen scan rate gives a simulated CV (see equation (3)).

10.1002/cphc.201900509

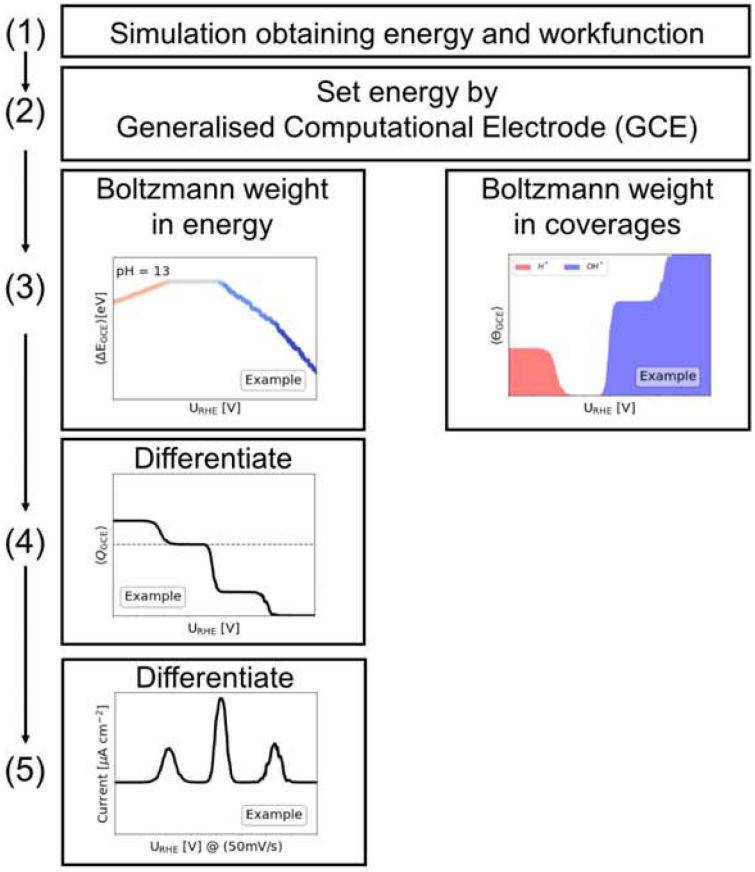

Figure 2: Flow diagram showing the principles used to obtain coverages and CVs from an interface model.

Cu(hkl) in alkaline media

The first calculations needed to create the theoretical CVs are simulation of the different coverages of H* and OH*. This set of simulation can represent CVs where electrolyte cation and anions have a minor influence. Specifically for the Cu system, we have previously shown that the binding energies are almost unaffected by the presence of cations[29].

From the simulations of H* and OH* on the three facets of Cu, in combination with the stepwise procedure of Figure 2, the coverages (noted $\langle\Theta_{\mathrm{GCE}}\rangle$) and theoretical CVs are obtained as shown in Figure 3**a-c** and Figure 3**d-f**, respectively.

Experimental CVs in NaOH are shown in Figure 3**g-i**. The Cu(111) facet is observed to have a double peak, the Cu(100) has one symmetric peak and the Cu(110) is rather featureless. This is similar to the experiments by *Schouten et al.*[20] We must note that CVs reported in the literature on Cu single-crystalline electrodes depend strongly on both the surface pre-treatment and the selected potential range [20, 23]. Recently, Engstfeld et al. showed that Cu(100) electrodes prepared by sputtering in ultra-high vacuum and annealing allowed the formation of highly-ordered surfaces [23]. The discrepancy between the reported CVs and those reported by Engstfeld et al. might be attributed to the presence of defects.

The experimental CVs can be interpreted by integrating the CV peaks as shown in Figure S1 for relevant anodic scans. Figure S1a reveals that the Cu(111) double peak corresponds roughly to about 3/12 or 4/12 ML charge. Figure S1b shows that the broad Cu(100) peak corresponds to 4/12 ML charge. For the case of Cu(111) and Cu(100) the experimental features allow for a fitting of the simulated states, and this illustrates the deviation of the OH* adsorption onset potential from simulations to experiment, with an approximate shift of 0.1 eV *per.* OH*.

The Cu(111) simulation in Figure 3**a** shows coverage, $\langle\Theta_{\mathrm{GCE}}\rangle$, of 0.33 ML (4/12 ML) OH*, which is similar to the experimental integrated double peak. However, the peak exhibits an earlier potential onset than the experimental results and the fit primarily move the OH* towards weaker binding.

The Cu(100) simulation in Figure 3**b** also reveals a coverage of 0.33 ML (4/12 ML) OH*, which is similar to the integration of the experimental peak. However, again the OH* binds too strong relative to experiments and by fitting the potential dependent increase in OH* coverage at more positive potential resemble the experimental results.

The OH* shift for Cu(111) is roughly 0.1 eV destabilization *per.* OH*, while for Cu(100) including only H* and OH* states the destabilization is larger (see Table S6). Another possibility for the experimental CV for Cu(100), is that combinations of H* and OH* are present. In Figure S6 the resulting simulation with combinations are shown with the fitting parameters in Table S8. This approach reveals close to similar destabilization energy *per.* OH* with Cu(111). Furthermore, it

illustrates that multiple solutions to experimentally observed adsorption/desorption phenomena from CVs exist and the difficulty of knowing the exact potentials and coverages.

The Cu(110) simulation exhibits a fixed OH coverage of 0.18 ML (3/16 ML) OH* over the investigated potential range, which resembles the flat experimental CV *i.e.* no fitting have been carried out.

Including only simulated H* and OH* intermediates in the interface to calculate theoretical CVs is shown to fit relatively well with the alkaline CVs of the Cu facets. Minor offsets in simulated and experimental peak positions are observed, which can be a result of deviating absolute DFT values.

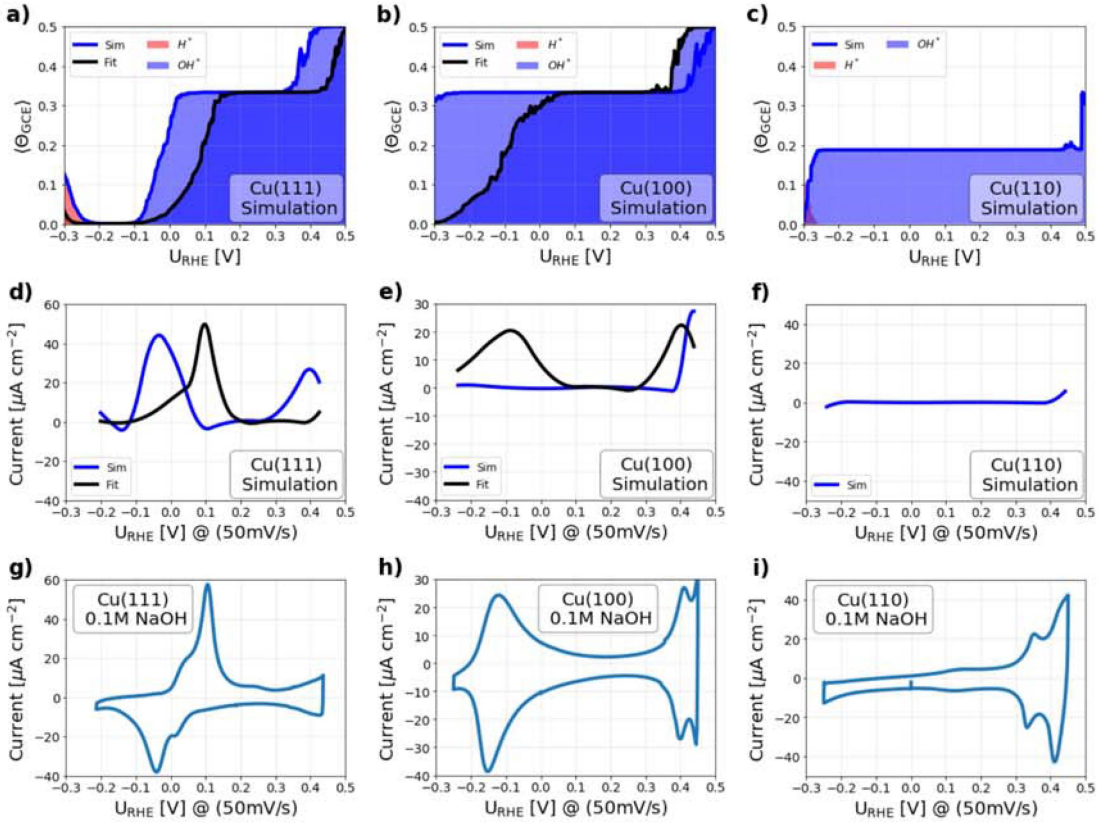

Figure 3: Simulations (blue) and fitting (black) of H* and OH* coverages (**a-c**), the derived CVs (**d-f**) and the experimental CVs (**g-i**) in alkaline (NaOH) for the three Cu(*hkl*) facets. Fitting parameters are given in Table S6.

Cu(hkl) in neutral media

For Cu(hkl) in neutral electrolytes, different H^*, OH^*, cation and anion configurations need to be considered. Previously[29] we have shown simulated results for phosphate and carbonate anions on the Cu(100) facet and moreover CO_3^* species has been experimentally observed on polycrystalline Cu in $KHCO_3$[45].

Figure 4 shows simulations and fits considering bicarbonate anions as well as H^* and OH^* together with the experimental CVs in $KHCO_3$ for the three Cu facets. The features of the experimental CVs change significantly with respect to the alkaline NaOH CVs presented in Figure 3.

The experimental CV on Cu(111) exhibits two separate peaks on the anodic scan and only one in the cathodic scan. The difference in anodic and cathodic scan led to speculation of reconstruction occur on the Cu(111) facet[46], which is not addressed here. Integrating of the two anodic peaks indicate that the first peak corresponds to 2/12 ML charge and the smaller second peak increases the charge coverage to 3/12 ML, see Figure S1c. The experimental CV for Cu(100) have a small decrease of charge over the potential range investigated, while Cu(110) exhibits a minor increase in charge due to a subtle feature around -0.05 V_{RHE}.

For the bicarbonate CV at Cu(111), the correction found for the alkaline Cu(111) CV is used for H^* and OH^* together with simulations of HCO_3^* and CO_3^* anions. Here the coverage of a CO_3^* anion is set to 2/12 ML to match the charge and the fact that the anion approximately takes up two sites at the surface. This suggests that initially one CO_3^* anion and one OH^* adsorps and at higher potentials additional adsorption of CO_3^* increases the total coverage. This results in simulation of two relatively sharp peaks with too much charge as compared to the experiment. When fitting is carried out, the CO_3^*, $2CO_3^*$ and $1OH^*$ states are all destabilized, allowing for a better fit to the experiment (fitting values is listed in Table S7). Another high coverage solution for CO_3^* anions can also be identified as shown in Figure S7, with the fitted values in Table S9. This also reproduces the experimental CV with a stronger average CO_3^* binding. Finally, a pure OH^* and H^* solution could also satisfy the experimental data, but this is neglected due to the observation of CO_3^* on polycrystaline Cu[45].

The Cu(100) simulation shows a surface covered by two CO_3^* anions giving rise to a relatively featureless CV comparable to the experiment. Only a small decay of a peak feature at low potential is shown from early adsorption of the carbonate anions and at high potentials from increased CO_3^* coverage.

The Cu(110) simulation shows first a 3/16 ML OH^* coverage (blue), followed by the adsorption of two CO_3^* anions. This gives rise to a peak in the simulated CV, whereas the experimental CV is flatter. The fitted model suggests that CO_3^* also binds stronger relative to that indicated by the simulations. However, still due to the finite size, the fit overestimates the CV peak size. Further, a pure OH^* and

H* solution could also have satisfied the experiment.

It is observed that adding carbonate anion species to the simulations agrees relatively well with the experimental CVs. The dual peak of Cu(111) is almost reproduced, the featureless Cu(100) CV arise due to a constant CO_3^* coverage and the Cu(110) deviate a bit.

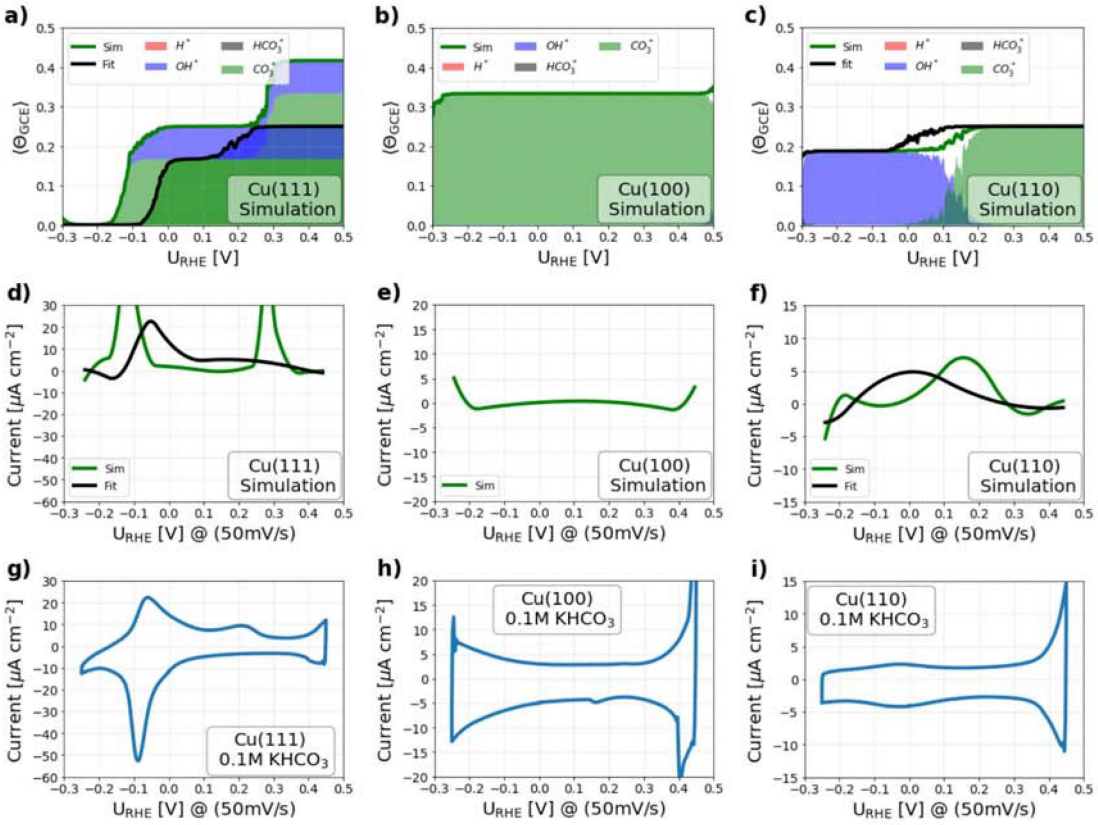

Figure 4: Simulations and fitting of H*, OH*, HCO_3^* and CO_3^* coverages (**a-c**), the derived CVs (**d-f**) and the experimental CVs (**g-i**) in neutral ($KHCO_3$) for the three Cu facets. The CO_3^* binds strongly hence poisoning the surface with respect to the OH* intermediates. Each CO_3^* has been set to cover two surface sites and fitting parameters for Cu(111) is given in Table S7.

Cu(hkl) in acidic media

For the acidic electrolyte, we investigate the influence of the strongly adsorbing Cl* species on the CVs of the Cu facets[43]. The previous investigations showed that the strong adsorbing Cl* anions can give rise to adsorption/desorption features at low overpotential[34, 35, 36] and importantly, the Cu surface is known to reconstruct in acidic conditions[33].

In this work, the experimental CVs for $HClO_4$+KCl electrolytes are shown in Figure 5. The Cu(111) and Cu(100) CVs are rather featureless CVs, while the Cu(110) CV has an almost symmetric peak observed at -0.1 V_{RHE}, corresponding to a change in charge of 1/16 ML, as integrated in Figure S1d.

The Cu(111) simulations show an initial coverage of 1/12 ML Cl* which increases up to 3/12 ML Cl* at -0.1 V_{RHE}. This increase gives rise to a broad region of positive current in the simulated CV. This broad feature does not exist in our experimental Cu(111) $HClO_4$+KCl CV. Instead, an increased negative current is observed from an assumed slow HER while having Cl* at the surface. Note that this irreversible current contribution from HER is not captured by the model i.e. this discrepancy between simulation and experimental CV is not surprising.

The Cu(100) simulations show a constant coverage of 3/12 ML Cl* in the investigated region. This results in a featureless (flat) simulated CV, which coincide well with that observed in the experiment. However, at higher potentials, the simulation suggest higher Cl* coverages, while the experimental CV could simply show oxidation/dissolution.

The Cu(110) simulations show an initial Cl* coverage of 3/16 ML which increases to 4/16 ML Cl*, giving rise to a simulated peak in the CV. This change in charge corresponds to the experimental CV, where the charge at the surface increases at -0.1 V_{RHE}. The fitted simulations show that only minor binding energy changes of Cl* move the simulated peak to fit the experiment. Note that this can also be a result of reconstructions at the surface by the strong Cl* interaction.

10.1002/cphc.201900509

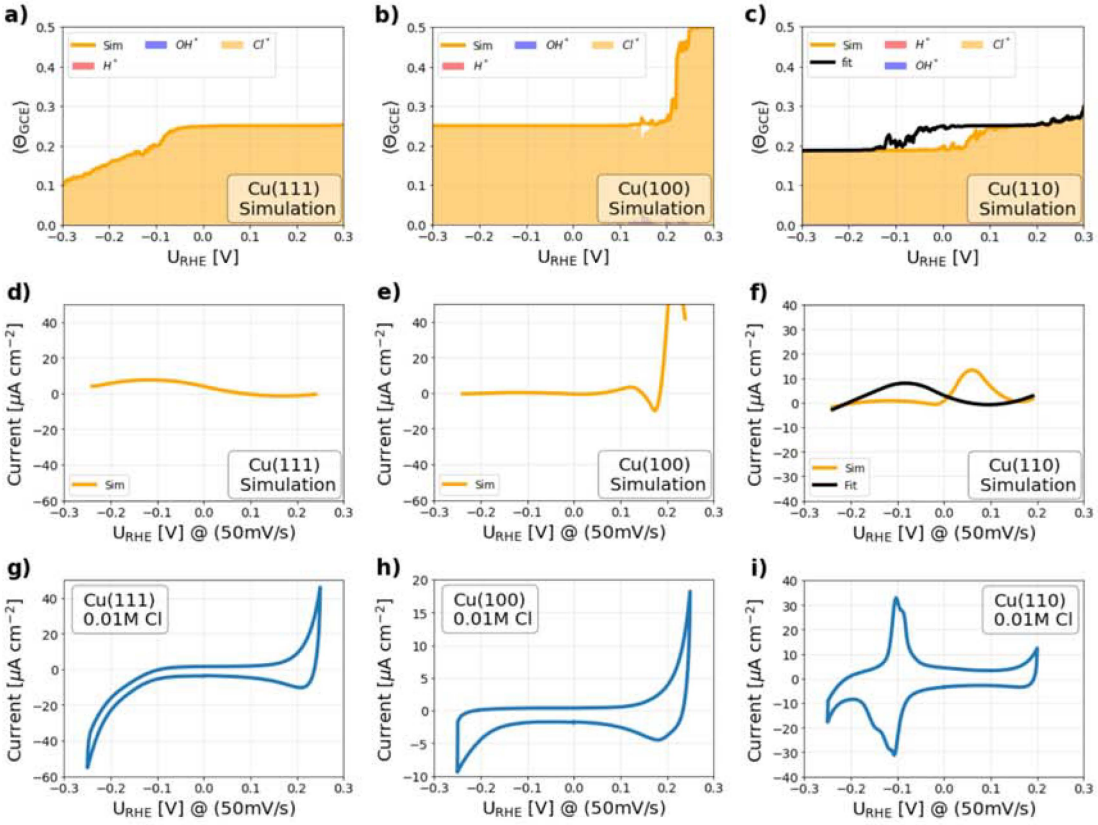

Figure 5: Simulations and fitting of H*, OH* and Cl* coverages (**a-c**), the derived CV (**d-f**) and the experimental CV (**g-i**) in acidic ($HClO_4$ + KCl) for the three Cu facets. The Cl anion, known to poison surfaces, bind strongly to the surface and has a poisoning effect with respect to OH*, which resemble the experiments.

Discussion

This work demonstrates how it is possible to utilize AIMD simulations of explicit electrolytes in contact with various surface facets to calculate the coverage of H^*, OH^* and different anions. Further, CVs have been derived and compared to experiments. A relatively good comparison is obtained, and by fitting the simulations, the origin of the differences is revealed. However, it is highly relevant to discuss: (*i*) the differences between AIMD and vacuum simulations, (*ii*) whether the workfunction reference is needed and (*iii*) differences between the proposed inactive $HClO_4$ and NaOH electrolytes.

(*i*) Is the AIMD, calculating the energy and workfunction to utilise the GCE scheme, really needed to obtain valid coverages on an RHE scale? In Figures S2, S3 and S4 the Computational Hydrogen Electrode (CHE)[2] surface Pourbaix diagrams and coverages are presented to be compared with the GCE result. A difference is that the CHE method has a step function feature of the coverages, which is similar to Pourbaix diagrams. The GCHE method has a smooth transition in coverages, which is based on the Boltzmann weighting of the states with different coverages and is the basis for deriving *ab initio* CVs. CVs can also be derived from CHE coverages, but only by an assumption on the transition between states (Langmuir isotherm or other). Comparing the coverages, the H^*, OH^* and to some extend Cl^*, the AIMD GCE and CHE results are relatively close to each other, while the HCO_3^* and CO_3^* anions exhibit significant differences. To investigate whether this is solely an effect of the AIMD water, the AIMD and vacuum energies of H^*, H_2O, Cl^*, CO^*, HCO_3^* and CO_3^* have been co-plotted as ΔE_{AIMD} *vs.* ΔE_{vacuum} in Figure 6. The figure elucidates that the H^*, Cl^* and CO^* energetics are similar in AIMD and vacuum, with minor differences of H_2O and, conversely, the CO_3^* exhibit very different AIMD and vacuum binding energy, with around 2.5 eV in difference. This could be a result of the references used to set the energy of CO_3^*, by the following equation:

$$CO + 2H_2O \rightarrow CO_3^* + 2H_2.$$

However, the references $CO(g) \rightarrow CO^*$, $H_2O(g) \rightarrow H_2O$ and $\frac{1}{2}H_2(g) \rightarrow H^*$ show that the strong binding of CO_3^* at low coverages is mainly a result of the AIMD water stabilisation, whereas high anion coverages may be troublesome in our current setup. Overall it shows that some intermediates/anions requires the explicit water stabilisation, in agreement with our previous work[29].

(*ii*) One could discuss whether it is necessary to calculate the workfunction and utilize this as a second reference point. The GCE scheme uses the workfunction to get structures at the intended potentials. We find that this is important for cases where the specific structure of the interface at a specific potential is needed and for coverages and CVs, when the energetics are close to each other (in the order of $\sim k_B T$). However, if the energetics of two comparable states are larger than $k_B T$, then the energetics dominate and the sampling of the workfunction is negligible for the purpose of CV and

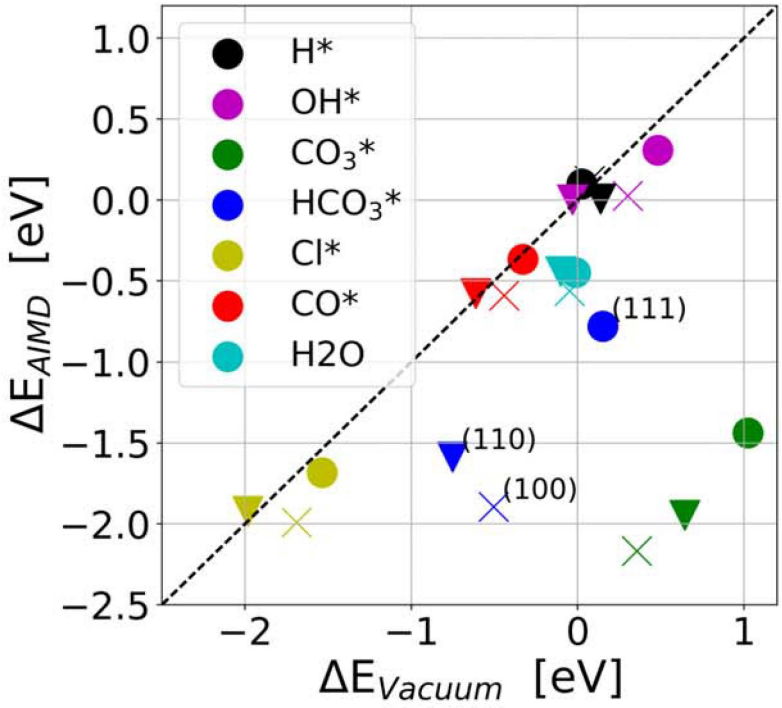

Figure 6: Comparison of binding energies between aqueous electrolyte AIMD simulations and vacuum simulation for single adsorbates. For both types of calculation the same references are used. Colors determine the adsorbate and the marker the Cu facet.

coverage plots.

(*iii*) Interestingly, the H* and OH* simulations seem to fit the alkaline CV for Cu. For Pt, the H* and OH* simulations have been suggested to fit the acidic CVs in the proposed inactive $HClO_4$ electrolyte[44]. However, there are differences between Cu and Pt. The workfunctions are $5.12 - 5.93$ eV and $4.53 - 5.10$ eV for Pt and Cu, respectively. Furthermore, the binding energies are different and the potential region of the CVs.

A comparison of the $HClO_4$ and NaOH electrolyte experiments is shown in Figure 7 for Cu(111) and Cu(100). The $HClO_4$ experiments show features close to the ionisation potential of $Cu \rightarrow Cu^{2+} + 2e^-$ (E_0=0.34V_{SHE}). The incorporation of the ClO_4^* anion to model the CV would be seemingly natural. However, trying to carry out the ClO_4^* anion calculation in the AIMD model reveals that the interface potential is below the stable ClO_4^* ion potential and the ion quickly breaks apart into other ions. Whether Cu surfaces really reduces the ClO_4^- ion to obtain a small ClO_x coverage is as of yet not known. Here, simulating H* and OH* in equilibrium at pH = 1 shows that this does not corresponds to the $HClO_4$ electrolyte CVs. In that instance the simulations rather exhibit the peak

features seen in the NaOH CVs. But retroactively comparing the NaOH and $HClO_4$ CVs does reveal similarities. The Cu(111) $HClO_4$ exhibits asymmetric peak at a higher RHE potential than NaOH which also display an asymmetric peak. Further, the Cu(100) exhibit a symmetric peak in both $HClO_4$ and NaOH. However, at different potentials and size. Hence, for both Cu(111) and Cu(100) the $HClO_4$ CVs could be fitted by only the H^* and OH^*, although with at large destabilisation of the OH^* as compared to the NaOH case. This could indicate a possible stabibilization of ClO_x species covering the surface, and that a certain potential is required for OH^* to displace these ClO_x species and increase the coverage. Thereby, leaving a similar, but smaller OH^* feature at high potential. However, this is only speculations.

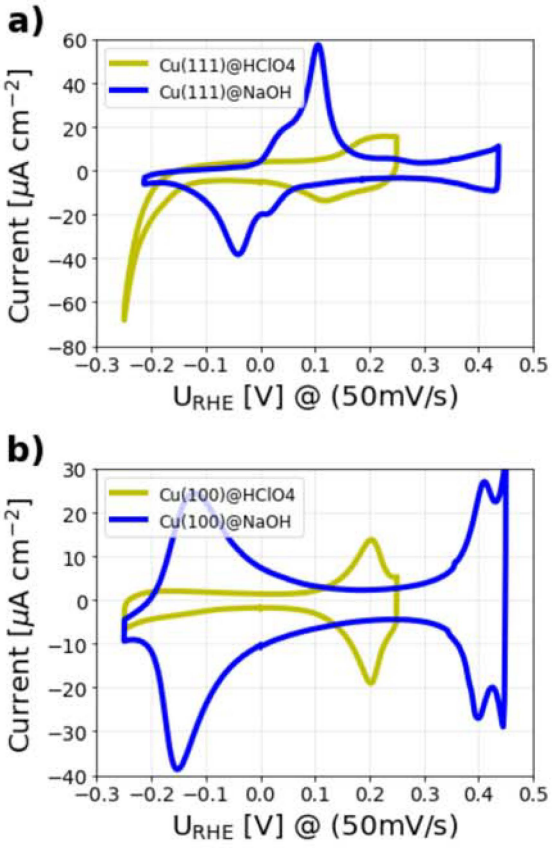

Figure 7: CV experiments of Cu(111) and Cu(100) in $HClO_4$ (acidic) and NaOH (alkaline) electrolytes.

Conclusion

It has been shown that the developed method can be used to derive coverages and CVs from simulated interface phase diagrams, which can be directly compared to experimental CVs. The results showed a relatively good comparison between calculated CVs at different electrolytes and pH conditions for the Cu(111), Cu(100) and Cu(110) facets. In alkaline conditions, the experiments were well described by only having OH^* on the surface, while in neutral bicarbonate conditions the surfaces for the Cu facets are covered by CO_3^* anions. It should be noted that the correct evaluation of anion adsorption in neutral pH widely relies on AIMD simulation, while only a small effect on H and OH adsorption is noted when compared to vacuum calculations. In acidic chloride containing media, the Cu surfaces exhibit significant Cl^* coverages. Notable differences between the simulated and experimental CVs were observed. These deviations were fitted when possible, but the deviations could also be a direct consequence of the limitations and assumptions listed in the introduction e.g. irreversible changes in the surface structures from reconstruction or oxidation ect.

Here we present a deeper understanding of what is present at the electrified interface, showing that we can obtain realistic electrochemical interfaces. Once having realistic electrochemical interfaces, electrochemical reactions can be studied more accurately by considering the relevant interface conditions that influence multiple reactions at acidic, neutral or alkaline conditions.

Methods

Electrochemical measurements

Prior to each experiment, Cu single crystal electrodes (MaTecK, 1 cm diameter, 99.999 %) with (100), (111) and (110) orientation were electropolished at 3 V *vs.* Ti foil for 10 s in a H_3PO_4/H_2SO_4 solution consisting of 130 mL H_3PO_4 (VWR, 85 $wt_{\%}$), 20 mL H_2SO_4 (VWR, 95 $wt_{\%}$) and 60 mL ultrapure water (Elga, 18.2 MΩ cm). The electrodes were then rinsed with ultrapure water and quickly transferred into the electrochemical cell. CV measurements were carried out at 50 mV/s in Ar-saturated (Air Liquide, N50) solutions containing 0.1 M NaOH (ACS. Reag. Merck), 0.1 M $KHCO_3$ (99.9%, Sigma-Aldrich), and 0.1 M $HClO_4$ + 0.01 M KCl (ACS. Reag. Merck). A custom-made electrochemical cell was used in a three electrode configuration, with a gold wire as a counter electrode and a reversible hydrogen electrode (RHE, HydroFlex, Gaskatel) as a reference electrode. A BioLogic 240 potentiostat was employed to control the electrode potential. All electrochemical measurements was done at room temperature in a hanging meniscus configuration.

Generalized Computational Electrode (GCE)

In order to generate the interface diagrams from our AIMD trajectories containing energy and work-function, we apply the Generalized Computational Hydrogen Electrode scheme.[40, 41]

The GCE[29] equation for different electrolyte investigations defines the energy of each state of the AIMD configurations for a given potential, concentration and pH as:

$$\begin{aligned}\Delta E_{\mathrm{GCE}}(n,x,\phi_{\mathrm{e^-}},\mathrm{pH}) =& E(n,x,\phi_{\mathrm{e^-}}) - \langle E(\{x,n\}=0)\rangle - x\mu_{\mathrm{X_{(g)}}} \\ & - n\tfrac{1}{2}\mu^0_{\mathrm{H_2}} - n\overbrace{(\phi_{\mathrm{SHE}} - \phi_{\mathrm{e^-}} - 2.3k_BT\mathrm{pH})}^{eU_{RHE}}, \text{ where } n=\{-6,..,6\}. \end{aligned} \quad (1)$$

Here the energy, ΔE_{GCE}, is a function of the number of protons n removed or added, the workfunction ϕ_{e^-}, pH ($\mathrm{U_{RHE}}$) and the number x of adsorbates X added at thermodynamic equilibrium conditions. μ denotes the chemical potential of a chemical species, ϕ_{SHE} is the defined standard hydrogen electrode (SHE) potential of 4.4 V on the absolute scale[48], k_B is Boltzmann's constant, T is the absolute temperature and $\langle E(\{n,x\}=0)\rangle$ is the reference energy.

In order to obtain the energetics and coverages of the interface at specific conditions determined by eq. (1), all the GCE energy states are Boltzmann-weighted by binning the data within a bin of chosen size as:

$$\langle A\rangle = \frac{1}{Z}\sum_{i=1}^{N} A_i \exp\left(\frac{-\Delta E_{\mathrm{GCE}}(n,x,\phi_{\mathrm{e^-}},\mathrm{pH})_i}{k_BT}\right), \quad A=\{\Delta E_{\mathrm{GCE}},\Theta_{\mathrm{GCE}}\}, \quad (2)$$

where Z is the partition function, N is the total number of states in the bin and $\langle A \rangle$ is the property of interest, in this case, the energy $\langle \Delta E_{\mathrm{GCE}} \rangle$ and the coverage $\langle \Theta_{\mathrm{GCE}} \rangle$.

Finally, the CV current is calculated as:

$$I = \frac{\mathrm{dQ}}{\mathrm{dt}} = \frac{\mathrm{dQ}}{\mathrm{dV}}\frac{\mathrm{dV}}{\mathrm{dt}} = \frac{\mathrm{dE}}{\mathrm{dV}}\frac{1}{\mathrm{dV}}\frac{\mathrm{dV}}{\mathrm{dt}} = \frac{\mathrm{dE}}{\mathrm{dV}}\frac{1}{\mathrm{dV}}\frac{\mathrm{dV}}{\mathrm{dt}}\frac{\mathrm{Q_{1ML}}}{\mathrm{e}} \tag{3}$$

where the $\frac{\mathrm{dE}}{\mathrm{dV}}\frac{1}{\mathrm{dV}}$ is the double differentiating of the phase diagram, $\frac{\mathrm{dV}}{\mathrm{dt}}$ is the CV scan speed (here 50 mV/s) and $\mathrm{Q_{1ML}}$ is the charge of one monolayer of the three facets. Here the charge, $\mathrm{Q_{1ML}}$, is calculated as the number of surface sites for each facet with a copper lattice constant of 3.6149Å, arriving at 283 μC/cm^2, 245 μC/cm^2 and 347 μC/cm^2 for Cu(111), Cu(100) and Cu(110), respectively. Carrying out the double differentiation on the Boltzmann weighted GCE states imposes considerable noise on the results, so for smoothness, the SciPy's built-in splines differentiation is used to create the CVs.

Computational details

Atomic structures were built with ASE[49]. The water interface models are constructed as orthogonal $(3\times4\times3)$, $(3\times4\times3)$ and $(2\times4\times3)$ unit cells for the (111), (100) and (110) copper facets, respectively, to obtain similar xy plane interfacial areas of the unit cells. Each water interface model consists of three water layers with a total of 24 H_2O molecules, which are allowed to move freely during the simulation, see Figure S8 for a side and top-view of the AIMD setup. An additional hexagonal water layer on top of the mobile aqueous phase is also kept fixed in order to keep the water density of the interface model constant and close to that of pure water. When atoms (protons or intermediates) are added and subtracted, the top water layer remains unchanged. Finally, the vacuum metal facet structures where created by removing the water layers from the water interface model.

The electronic structure calculations are carried out at the Generalized Gradient Approximation Density Functional Theory (GGA-DFT) level with the projector-augmented wave method as implemented in GPAW[50]. Different levels of electronic structure calculation were employed: (1) Finite-difference calculations are carried out for vacuum binding energies using $(4 \times 4 \times 1)$ k-points, the RPBE[51] functional and a 0.18 Å grid spacing. (2) The water/copper interface is modeled by AIMD at a constant temperature of 300 K (using *Berendsen*[52] NVT dynamics, with a timestep of 0.5 fs and a time temperature cooling constant of 100 fs) as implemented in GPAW. To achieve thermal equilibration and a sufficient number of states for the GCE approach, the electronic structure calculations are carried out by RPBE[51] calculations in LCAO mode with a grid spacing of 0.18 Å at the gamma point. In Figure S9 the water AIMD runs of Cu(111), Cu(100) and Cu(110) is displayed with total energies and workfunction sampling.

Acknowledgment

This work was supported by Climate-KIC under the EnCO$_2$re project, the Carlsberg Foundation (grant CF15-0165) and the Innovation Fund Denmark (grand solution ProActivE 5124-00003A). JHS acknowledge a travel grant from the Royal Swedish Academy of Science and founding from the Swedish Nuclear Fuel and Waste Management Company (SKB). ECdS gratefully acknowledge support from the Brazilian agencies: Fundação de Amparo à Pesquisa do Estado de Minas Gerais (FAPEMIG), Conselho Nacional para o Desenvolvimento Científico e Technológico (CNPq) and Coordenação de Aperfeiçoamento de Pessoal de Ensino Superior (CAPES). RAA and BRC appreciate the financial support of the european research council (ERC-725915, OPERANDOCAT). We thank professor Lars G. M. Pettersson for valuable discussions.

Competing interests

The authors declare no competing financial interest.

Keywords

Cyclic Voltammetry, Electrochemistry, Electrochemical interface models, Ab Initio Molecular Dynamics, Cu single crystals.

Table of Contents

Here a method is presented to move from thermodynamic realistic interface structures obtained from ab initio simulations to cyclic voltammograms and visa versa. The method have been validated by direct comparison to experimental cyclic voltammograms and an almost one-to-one mapping is observed from simulation to experiments.

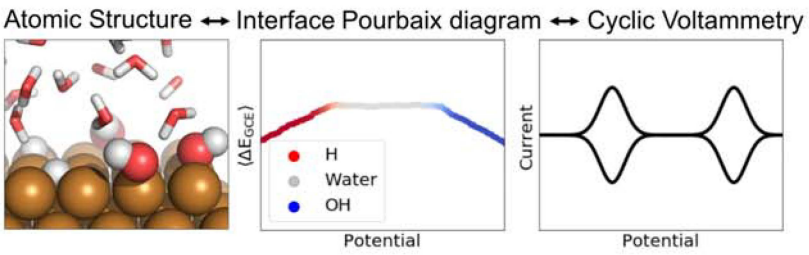

References

[1] Vojislav R. Stamenkovic, Dusan Strmcnik, Pietro P. Lopes, and Nenad M. Markovic. Energy and fuels from electrochemical interfaces. *Nature Materials*, 16(57), 2016.

[2] Eva M. Fernández, Poul G. Moses, Anja Toftelund, Heine A. Hansen, José I. Martínez, Frank Abild-Pedersen, Jesper Kleis, Berit Hinnemann, Jan Rossmeisl, Thomas Bligaard, and Jens K. Nørskov. Scaling relationships for adsorption energies on transition metal oxide, sulfide, and nitride surfaces. *Angewandte Chemie International Edition*, 47(25):4683–4686, 2008.

[3] Federico Calle-Vallejo, David Loffreda, Marc T. M. Koper, and Philippe Sautet. Introducing structural sensitivity into adsorption-energy scaling relations by means of coordination numbers. *Nature Chemistry*, 7:403, 2015.

[4] J. K. Nørskov, T. Bligaard, J. Rossmeisl, and C. H. Christensen. Towards the computational design of solid catalysts. *Nature Chemistry*, 1:37, 2009.

[5] J. K. Nørskov, T. Bligaard, A. Logadottir, J. R. Kitchin, J. G. Chen, S. Pandelov, and U. Stimming. Trends in the exchange current for hydrogen evolution. *Journal of The Electrochemical Society*, 152(3):J23–J26, 2005.

[6] Isabela C. Man, Hai-Yan Su, Federico Calle-Vallejo, Heine A. Hansen, José I. Martínez, Nilay G. Inoglu, John Kitchin, Thomas F. Jaramillo, Jens K. Nørskov, and Jan Rossmeisl. Universality in oxygen evolution electrocatalysis on oxide surfaces. *ChemCatChem*, 3(7):1159–1165, 2011.

[7] Olaf M. Magnussen and Axel Groß. Toward an atomic-scale understanding of electrochemical interface structure and dynamics. *Journal of the American Chemical Society*, 141(12):4777–4790, 2019.

[8] Pietro P. Lopes, Dusan Strmcnik, Jakub S. Jirkovsky, Justin G. Connell, Vojislav Stamenkovic, and Nenad Markovic. Double layer effects in electrocatalysis: The oxygen reduction reaction and ethanol oxidation reaction on Au(111), Pt(111) and Ir(111) in alkaline media containing Na and Li cations. *Catalysis Today*, 262:41 – 47, 2016. Electrocatalysis.

[9] T.J. Schmidt, V. Stamenkovic, M. Arenz, N.M. Markovic, and P.N. Ross. Oxygen electrocatalysis in alkaline electrolyte: Pt(hkl), Au(hkl) and the effect of Pd-modification. *Electrochimica Acta*, 47(22):3765 – 3776, 2002.

[10] Kenji Sashikata, Nagakazu Furuya, and Kingo Itaya. In situ electrochemical scanning tunneling microscopy of single-crystal surfaces of Pt(111), Rh(111), and Pd(111) in aqueous sulfuric acid

solution. *Journal of Vacuum Science & Technology B: Microelectronics and Nanometer Structures Processing, Measurement, and Phenomena*, 9(2):457–464, 1991.

[11] V. Climent and Juan Feliu. Thirty years of platinum single crystal electrochemistry. *Journal of Solid State Electrochemistry*, 15(8):1297–1315, 2011.

[12] Kim D. Jensen, Jakub Tymoczko, Jan Rossmeisl, Aliaksandr S. Bandarenka, Ib Chorkendorff, María Escudero-Escribano, and Ifan E. L. Stephens. Elucidation of the oxygen reduction volcano in alkaline media using a copper-platinum(111) alloy. *Angewandte Chemie International Edition*, 57(11):2800–2805, 2018.

[13] N.S Marinković, J.S Marinković, and R.R Adžić. In situ infrared spectroscopic investigations of sulfate adsorption at the Ag(111) electrode surface. *Journal of Electroanalytical Chemistry*, 467(1):291 – 298, 1999.

[14] B.M Jovic, V.D Jovic, and G.R Stafford. Cyclic voltammetry on Ag(111) and Ag(100) faces in sodium hydroxide solutions. *Electrochemistry Communications*, 1(6):247 – 251, 1999.

[15] Ludwig A. Kibler, Ahmed M. El-Aziz, Rüdiger Hoyer, and Dieter M. Kolb. Tuning reaction rates by lateral strain in a palladium monolayer. *Angewandte Chemie International Edition*, 44(14):2080–2084, 2005.

[16] Alberto Ganassin, Paula Sebastián, Víctor Climent, Wolfgang Schuhmann, Aliaksandr S. Bandarenka, and Juan Feliu. On the pH dependence of the potential of maximum entropy of Ir(111) electrodes. *Scientific Reports*, 7(1246), 2017.

[17] S.R. Brankovic, N.S. Marinkovic, J.X. Wang, and R.R. Adžić. Carbon monoxide oxidation on bare and Pt-modified Ru(1010) and Ru(0001) single crystal electrodes. *Journal of Electroanalytical Chemistry*, 532(1):57 – 66, 2002.

[18] V.D. Jović and B.M. Jović. Eis and differential capacitance measurements onto single crystal faces in different solutions: Part ii: Cu(111) and Cu(100) in 0.1 M NaOH. *Journal of Electroanalytical Chemistry*, 541:13 – 21, 2003.

[19] V.D. Jović and B.M. Jović. Surface reconstruction during the adsorption/desorption of OH species onto Cu(111) and Cu(100) in 0.1 M NaOH solution. *Journal of the Serbian Chemical Society*, 531, 2002.

[20] Klaas Jan P. Schouten, Elena Pérez Gallent, and Marc T.M. Koper. The electrochemical characterization of copper single-crystal electrodes in alkaline media. *Journal of Electroanalytical Chemistry*, 699:6 – 9, 2013.

[21] V. Maurice, H.-H. Strehblow, and P. Marcus. In situ STM study of the initial stages of oxidation of Cu(111) in aqueous solution. *Surface Science*, 458(1):185 – 194, 2000.

[22] Aneta ŁLukomska and Jerzy Sobkowski. Potential of zero charge of monocrystalline copper electrodes in perchlorate solutions. *Journal of Electroanalytical Chemistry*, 567(1):95 – 102, 2004.

[23] Albert K Engstfeld, Thomas Magaard, Sebastian Horch, Ib Chorkendorff, and Ifan Erfyl Lester Stephens. Polycrystalline and single crystal Cu electrodes: influence of experimental conditions on the electrochemical properties in alkaline media. *Chemistry - A European Journal*, 24(67):17743–17755, 2018.

[24] Y. Hori, A. Murata, and R. Takahashi. Formation of hydrocarbons in the electrochemical reduction of carbon dioxide at a copper electrode in aqueous solution. *Journal of the Chemical Society, Faraday Transactions*, 85:2309–2326, 1989.

[25] A. Bagger, W. Ju, A. S. Varela, P. Strasser, and J. Rossmeisl. Electrochemical CO2 reduction: A classification problem. *ChemPhysChem*, 18(22):3266–3273, 2017.

[26] Dunfeng Gao, Ioannis Zegkinoglou, Nuria J. Divins, Fabian Scholten, Ilya Sinev, Philipp Grosse, and Beatriz Roldan Cuenya. Plasma-activated copper nanocube catalysts for efficient carbon dioxide electroreduction to hydrocarbons and alcohols. *ACS Nano*, 11(5):4825–4831, 2017.

[27] Dunfeng Gao, Ian T. McCrum, Shyam Deo, Yong-Wook Choi, Fabian Scholten, Weiming Wan, Jingguang G. Chen, Michael J. Janik, and Beatriz Roldan Cuenya. Activity and selectivity control in CO2 electroreduction to multicarbon products over CuOx catalysts via electrolyte design. *ACS Catalysis*, 8(11):10012–10020, 2018.

[28] K. J. P. Schouten, Z. Qin, E. P. Gallent, and M. T. M. Koper. Two pathways for the formation of ethylene in CO reduction on single-crystal copper electrodes. *Journal of the American Chemical Society*, 134(24):9864–9867, 2012.

[29] Alexander Bagger, Logi Arnarson, Martin H. Hansen, Eckhard Spohr, and Jan Rossmeisl. Electrochemical CO reduction: A property of the electrochemical interface. *Journal of the American Chemical Society*, 141(4):1506–1514, 2019.

[30] Hideshi Ooka, Marta C. Figueiredo, and Marc T. M. Koper. Competition between hydrogen evolution and carbon dioxide reduction on copper electrodes in mildly acidic media. *Langmuir*, 33(37):9307–9313, 2017.

[31] Meenesh R. Singh, Youngkook Kwon, Yanwei Lum, Joel W. Ager, and Alexis T. Bell. Hydrolysis of electrolyte cations enhances the electrochemical reduction of CO2 over Ag and Cu. *Journal of the American Chemical Society*, 138(39):13006–13012, 2016. PMID: 27626299.

[32] Y. Hori, I. Takahashi, O. Koga, and N. Hoshi. Electrochemical reduction of carbon dioxide at various series of copper single crystal electrodes. *Journal of Molecular Catalysis A: Chemical*, 199(1):39 – 47, 2003. Special Issue dedicated to Professor Juro Horiuti in commemoration of his centennial birthday and his contribution to science.

[33] H. Matsushima, A. Taranovskyy, C. Haak, Y. Gründer, and O. M. Magnussen. Reconstruction of Cu(100) electrode surfaces during hydrogen evolution. *Journal of the American Chemical Society*, 131(30):10362–10363, 2009.

[34] J. Inukai, Y. Osawa, and K. Itaya. Adlayer structures of chlorine, bromine, and iodine on Cu(111) electrode in solution: In-situ STM and ex-situ LEED studies. *The Journal of Physical Chemistry B*, 102(49):10034–10040, 1998.

[35] Sang-Eun Bae and Andrew A. Gewirth. In situ EC-STM studies of MPS, SPS, and chloride on Cu(100): Structural studies of accelerators for dual damascene electrodeposition. *Langmuir*, 22(25):10315–10321, 2006.

[36] M.R. Vogt, A. Lachenwitzer, O.M. Magnussen, and R.J. Behm. In-situ STM study of the initial stages of corrosion of Cu(100) electrodes in sulfuric and hydrochloric acid solution. *Surface Science*, 399(1):49 – 69, 1998.

[37] B Beverskog and Ignasi Puigdomenech. Revised pourbaix diagrams for copper at 25 to 300°c. *Journal of The Electrochemical Society*, 144, 10 1997.

[38] J. A. Herron, Y. Morikawa, and M. Mavrikakis. Ab initio molecular dynamics of solvation effects on reactivity at electrified interfaces. *Proceedings of the National Academy of Sciences*, 113(34):E4937–E4945, 2016.

[39] Maryam Naderian and Axel Groß. From single molecules to water networks: Dynamics of water adsorption on Pt(111). *The Journal of Chemical Physics*, 145(9):094703, 2016.

[40] J. Rossmeisl, K. Chan, R. Ahmed, V. Tripkovic, and M. E. Bjørketun. pH in atomic scale simulations of electrochemical interfaces. *Phys. Chem. Chem. Phys.*, 15:10321–10325, 2013.

[41] M. H. Hansen and J. Rossmeisl. pH in grand canonical statistics of an electrochemical interface. *The Journal of Physical Chemistry C*, 120(51):29135–29143, 2016.

[42] Florian Gossenberger, Tanglaw Roman, and Axel Groß. Hydrogen and halide co-adsorption on Pt(111) in an electrochemical environment: a computational perspective. *Electrochimica Acta*, 216:152 – 159, 2016.

[43] Florian Gossenberger, Tanglaw Roman, and Axel Groß. Equilibrium coverage of halides on metal electrodes. *Surface Science*, 631:17 – 22, 2015. Surface Science and Electrochemistry - 20 years later.

[44] M. H. Hansen, A. Nilsson, and J. Rossmeisl. Modelling pH and potential in dynamic structures of the water/Pt(111) interface on the atomic scale. *Phys. Chem. Chem. Phys.*, 19:23505–23514, 2017.

[45] Yu Katayama, Francesco Nattino, Livia Giordano, Jonathan Hwang, Reshma R. Rao, Oliviero Andreussi, Nicola Marzari, and Yang Shao-Horn. An in situ surface-enhanced infrared absorption spectroscopy study of electrochemical CO2 reduction: Selectivity dependence on surface C-bound and O-bound reaction intermediates. *The Journal of Physical Chemistry C*, 123(10):5951–5963, 2019.

[46] Youn-Geun Kim, Jack Hess Baricuatro, Alnald Javier, John Mathew Gregoire, and Manuel P. Soriaga. The evolution of the polycrystalline copper surface, first to Cu(111) and then to Cu(100), at a fixed CO2RR potential: A study by operando EC-STM. *Langmuir*, 30(50):15053–15056, 2014.

[47] J. K. Nørskov, J. Rossmeisl, A. Logadottir, L. Lindqvist, J. R. Kitchin, T. Bligaard, and H. Jónsson. Origin of the overpotential for oxygen reduction at a fuel-cell cathode. *The Journal of Physical Chemistry B*, 108(46):17886–17892, 2004.

[48] Sergio Trasatti. The absolute electrode potential: an explanatory note (recommendations 1986). *Journal of Electroanalytical Chemistry and Interfacial Electrochemistry*, 209(2):417 – 428, 1986.

[49] A. H. Larsen, J. J. Mortensen, J. Blomqvist, I. E. Castelli, R. Christensen, M. Dułak, J. Friis, M. N. Groves, B. Hammer, C. Hargus, E. D. Hermes, P. C. Jennings, P. B. Jensen, J. Kermode, J. R. Kitchin, E. L. Kolsbjerg, J. Kubal, K. Kaasbjerg, S. Lysgaard, J. B. Maronsson, T. Maxson, T. Olsen, L. Pastewka, A. Peterson, C. Rostgaard, J. Schiøtz, O. Schütt, M. Strange, K. S. Thygesen, T. Vegge, L. Vilhelmsen, M. Walter, Z. Zeng, and K. W. Jacobsen. The atomic simulation environment - a python library for working with atoms. *Journal of Physics: Condensed Matter*, 29(27):273002, 2017.

[50] J. Enkovaara, C. Rostgaard, J. J. Mortensen, J. Chen, M. Du|ak, L. Ferrighi, J. Gavnholt, C. Glinsvad, V. Haikola, H. A. Hansen, H. H. Kristoffersen, M. Kuisma, A. H. Larsen, L. Lehtovaara, M. Ljungberg, O. Lopez-Acevedo, P. G. Moses, J. Ojanen, T. Olsen, V. Petzold, N. A.

Romero, J. Stausholm-Møller, M. Strange, G. A. Tritsaris, M. Vanin, M. Walter, B. Hammer, H. Häkkinen, G. K. H. Madsen, R. M. Nieminen, J. K. Nørskov, M. Puska, T. T. Rantala, J. Schiøtz, K. S. Thygesen, and K. W. Jacobsen. Electronic structure calculations with GPAW: a real-space implementation of the projector augmented-wave method. *Journal of Physics: Condensed Matter*, 22(25):253202, 2010.

[51] B. Hammer, L. B. Hansen, and J. K. Nørskov. Improved adsorption energetics within density-functional theory using revised Perdew-Burke-Ernzerhof functionals. *Phys. Rev. B*, 59:7413–7421, 1999.

[52] H. J. C. Berendsen, J. P. M. Postma, W. F. van Gunsteren, A. DiNola, and J. R. Haak. Molecular dynamics with coupling to an external bath. *The Journal of Chemical Physics*, 81(8):3684–3690, 1984.

Supporting Information

Ab Initio Cyclic Voltammetry on Cu(111), Cu(100) and Cu(110) in Acidic, Neutral and Alkaline

Alexander Bagger, Rosa M. Arán-Ais, Joakim Halldin Stenlid, Egon Campos dos Santos, Logi Arnarson, Kim Degn Jensen, María Escudero-Escribano, Beatriz Roldan Cuenya and Jan Rossmeisl

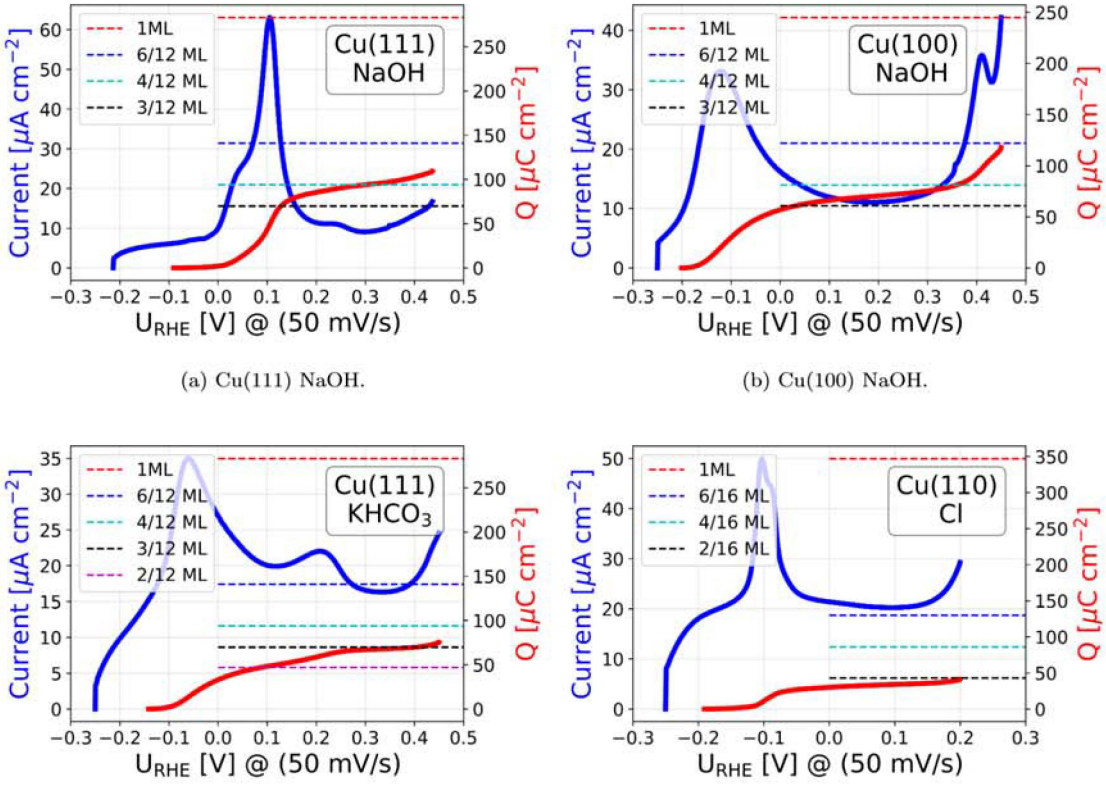

(a) Cu(111) NaOH.

(b) Cu(100) NaOH.

(c) Cu(111) $KHCO_3$.

(d) Cu(110) Cl.

Figure S1: Shows the anodic CV (blue) and the integration (red) of anodic CV scans on relevant Cu facets and electrolytes. The integration can be compared to charges lines for each facet obtained as the charge of 1ML correspond to 283 $\mu C/cm^2$, 245 $\mu C/cm^2$ and 347 $\mu C/cm^2$ for Cu(111), Cu(100) and Cu(110), respectively. For Cu(110) having rows of atoms, both the top and bottom rows have been used to describe 1 ML, given the highest charge per cm^2.

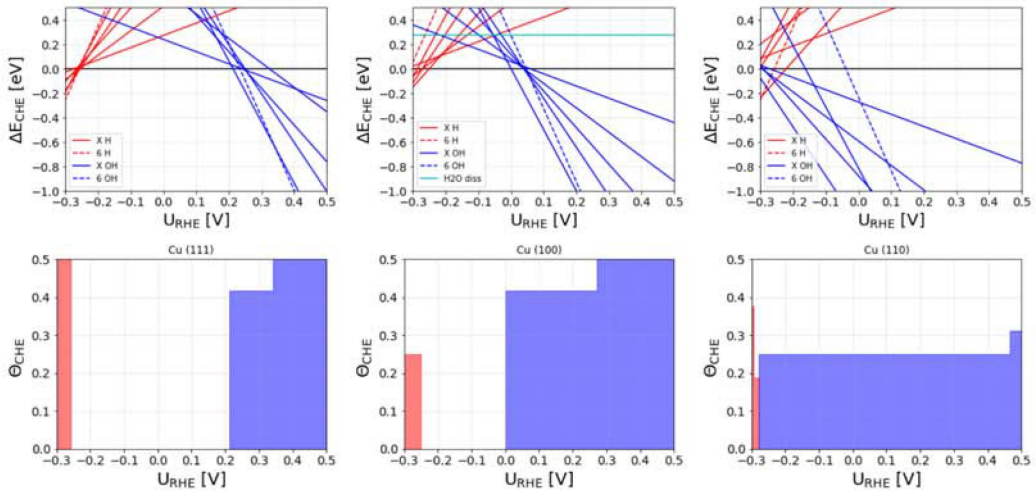

Figure S2: Vacuum binding energies and utilization of the CHE to create surface Pourbaix diagram and coverages as a function of potential. H* and OH* structures from the AIMD simulations is used without the water.

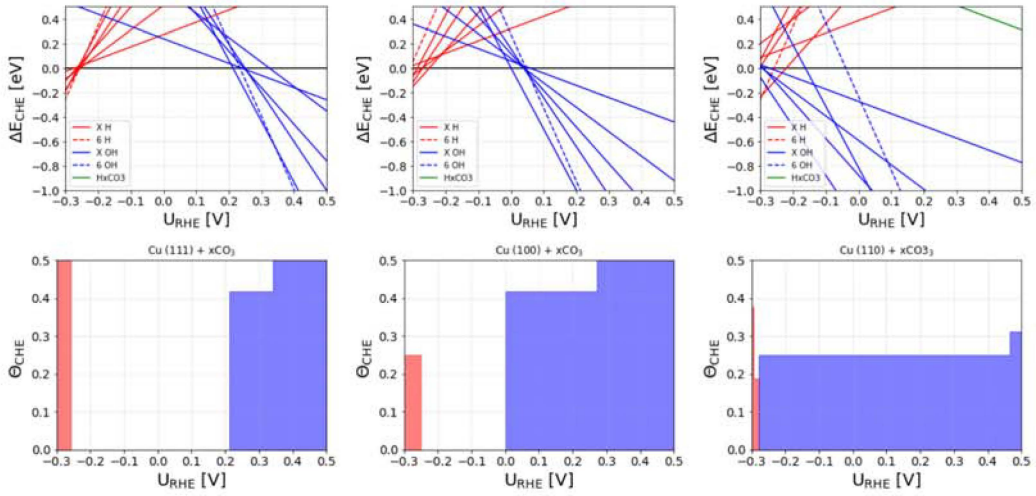

Figure S3: Vacuum binding energies and utilization of the CHE to create surface Pourbaix diagram and coverages as a function of potential. H*, OH*, HCO_3^* and CO_3 structures from the AIMD simulations is used without the water. Note that HCO_3^* and CO_3 structures are included, they are just so unstable that they are not visible.

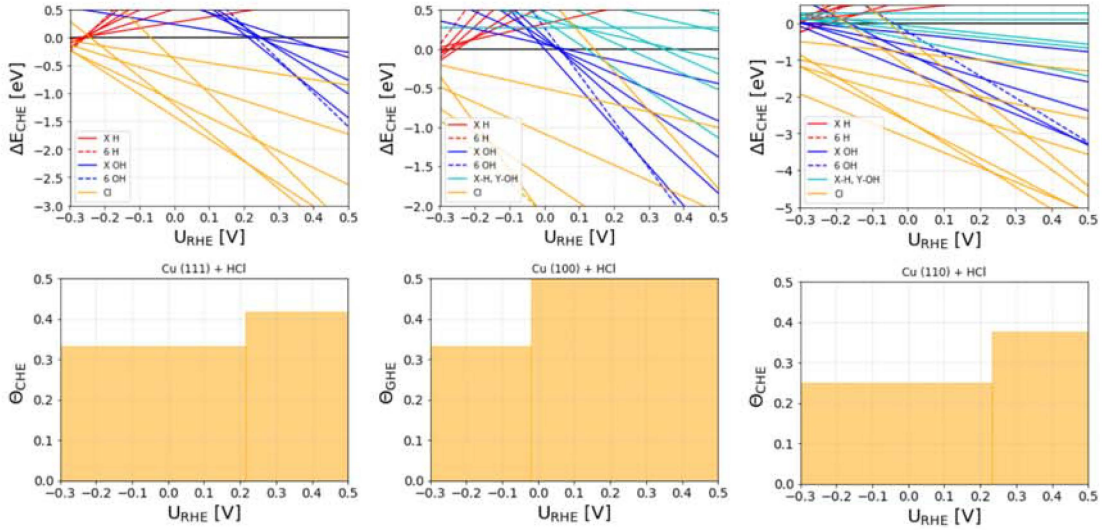

Figure S4: Vacuum binding energies and utilization of the CHE to create surface Pourbaix diagram and coverages as a function of potential. H*, OH* and Cl* structures from the AIMD simulations is used without the water.

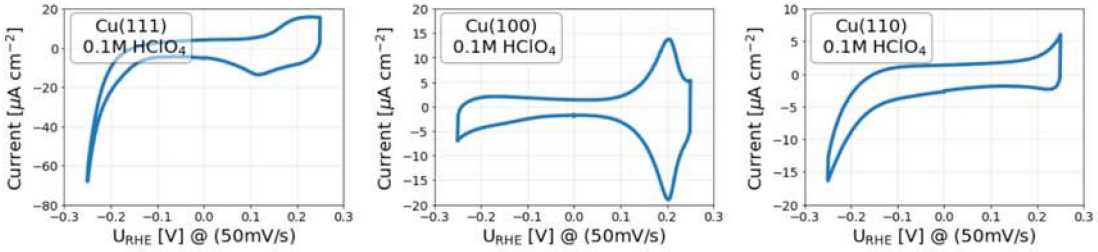

Figure S5: Experimental CVs in $HClO_4$ solutions on Cu(111), Cu(100) and Cu(110).

Table S1: Thermodynamic data used from Atkins [1] to set the energy of Cl^-(aq) with respect to Cl_2(g).

	$1/2\ Cl_2$(g)	→	Cl^-(aq)
ΔG	1/2 * 0 kJ/mol		-131.23 kJ/mol
			-1.36eV

Table S2: Thermodynamic data used from Atkins [1] to set the energy of Cl^* with respect to Cl_2(g). We assume that at the surface the chlorine has zero entropy.

	$1/2\ Cl_2$(g)	→	Cl^*
-TΔS	-1/2*0.69 eV		0 eV
ZPE	0.049 eV		0.021 eV
ΔG_2			**0.317 eV**

Table S3: Thermodynamic data used for carbonate at 1M and pH=0.

	H_2CO_3(aq)	HCO_3^-(aq)	CO_3^{2-}(aq)
G [kJ/mol]	-623.08 kJ/mol	-586.77 kJ/mol	-527.81 kJ/mol

When including dissolved CO_2(aq):

$$\frac{[H^+][HCO_3^-]}{[H_2CO_3]} = 4.4 \times 10^{-7}, \quad \frac{[H^+][CO_3^{2-}]}{[HCO_3^-]} = 4.69 \times 10^{-11}$$

At all pH

$$G_{H_2CO_3} = G_{HCO_3^- + H^+} = G_{CO_3^{2-} + 2H^+}$$

Hence at pH=8.3 and 0.1M, assuming majority of HCO_3^- and H_2CO_3

$$4.4 \times 10^{-7} = \frac{[H^+][HCO_3^-]}{[H_2CO_3]} = \frac{10^{-8.3} \times x}{0.1 - x} \leftrightarrow x = 0.09887$$

$$G_{HCO_3^- + H^+} = -586.77\text{kJ/mol} + k_B T ln([0.09887]) + k_B T ln([10^{-8.3}]) = -640.21\text{kJ/mol}$$

Table S4: Thermodynamic data used from Atkins [1] to set the energy of H_2CO_3 with respect to CO(g), H_2O(g) and H_2(g).

	CO(g)	+	2 * H_2O(g)	→	H_2CO_3 (aq)	+	H_2(g)
ΔG	-137.17 kJ/mol		-2 * 228.57 kJ/mol		-640.21 kJ/mol		0 kJ/mol
ΔG_1							**-0.48 eV**

Table S5: Thermodynamic data used from Atkins [1] and Nørskov et. al.[2]to set the energy of HCO_3^* and CO_3^* with respect to CO(g), H_2O(g) and H_2(g). We assume that at the surface the carbonate has zero entropy.

	CO(g)	+	2 * H_2O(g)	→	HCO_3^*	+	3/2 H_2(g)	
-TΔS	-0.612 eV		-2 * 0.67 eV		0 eV		-3/2* 0.41 eV	
ZPE	0.13 eV		2 * 0.56 eV		0.728 eV		3/2 * 0.27 eV	
ΔG_2								**1.22 eV**

	CO(g)	+	2 * H_2O(g)	→	CO_3^*	+	2 H_2(g)	
-TΔS	-0.612 eV		-2 * 0.67 eV		0 eV		-2 0.41 eV	
ZPE	0.13 eV		2 * 0.56 eV		0.425 eV		2 * 0.27 eV	
ΔG_2								**0.85 eV**

Cu(111) NaOH	E_{fit} [eV]
$E(-1, p, \phi_{e^-})$	-0.072
$E(-2, p, \phi_{e^-})$	0.192
$E(-3, p, \phi_{e^-})$	0.243
$E(-4, p, \phi_{e^-})$	0.402
$E(-5, p, \phi_{e^-})$	8.264
$E(-6, p, \phi_{e^-})$	0.594
$E(n = \{1, .., 6\}, p, \phi_{e^-})$	0.080

Cu(100) NaOH	E_{fit} [eV]
$E(-1, p, \phi_{e^-})$	0.077
$E(-2, p, \phi_{e^-})$	27.98
$E(-3, p, \phi_{e^-})$	0.781
$E(-4, p, \phi_{e^-})$	1.135
$E(-5, p, \phi_{e^-})$	31.21
$E(-6, p, \phi_{e^-})$	1.00
$E(n = \{1, .., 6\}, p, \phi_{e^-})$	32.72

Table S6: Fitting parameters obtained from fitting AIMD states to experimental NaOH CVs for Cu(111) and Cu(100).

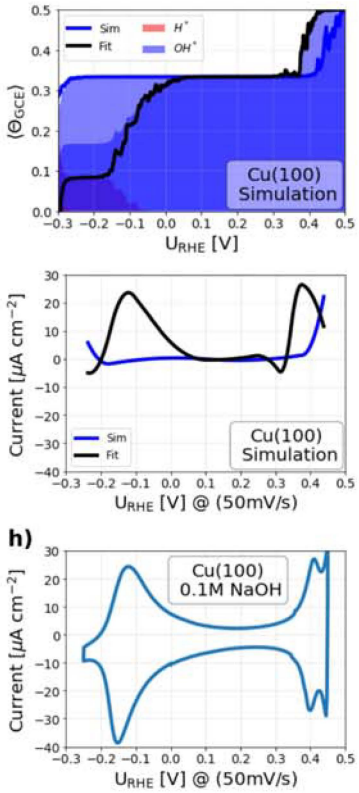

Figure S6: Simulations and fitting of H* and OH* coverages including combinations for alkaline (NaOH) for the Cu(100) facet. Fitting parameters are given in Table S8.

Cu(111) KCO_3	E_{fit}[eV]
$E(-1, p, \phi_{e^-})$	-0.072
$E(-2, p, \phi_{e^-})$	0.192
$E(-3, p, \phi_{e^-})$	0.243
$E(-4, p, \phi_{e^-})$	0.402
$E(-5, p, \phi_{e^-})$	8.264
$E(-6, p, \phi_{e^-})$	0.594
$E(n = \{1, .., 6\}, p, \phi_{e^-})$	0.080
$E(\{1, 2, 3\}HCO3, p, \phi_{e^-})$	0.0
$E(CO3, p, \phi_{e^-})$	0.0
$E(2CO3, p, \phi_{e^-})$	0.0

Cu(111) KCO_3	E_{fit} [eV]
$E(-1, p, \phi_{e^-})$	0.23
$E(-2, p, \phi_{e^-})$	63.3
$E(-3, p, \phi_{e^-})$	63.3
$E(-4, p, \phi_{e^-})$	63.5
$E(-5, p, \phi_{e^-})$	71.4
$E(-6, p, \phi_{e^-})$	63.7
$E(n = \{1, .., 6\}, p, \phi_{e^-})$	55.3
$E(\{1, 2, 3\}HCO3, p, \phi_{e^-})$	63.1
$E(CO3, p, \phi_{e^-})$	0.19
$E(2CO3, p, \phi_{e^-})$	52.9

Table S7: Fitting parameters obtained from fitting AIMD states to experimental $KHCO_3$ CV for Cu(111). Left show prior with NaOH fitting parameters and right shows after fitting the CV.

Cu(100) NaOH	E_{fit} [eV]
$E(-1, p, \phi_{e^-})$	0.195
$E(-2, p, \phi_{e^-})$	0.115
$E(-3, p, \phi_{e^-})$	0.310
$E(-4, p, \phi_{e^-})$	0.642
$E(-5, p, \phi_{e^-})$	10.95
$E(-6, p, \phi_{e^-})$	0.514
$E(n = \{1, .., 6\}, p, \phi_{e^-})$	-0.100

Table S8: Cu(100) fitting parameters for combinations of OH^* and H^* obtained from fitting AIMD states to experimental CV.

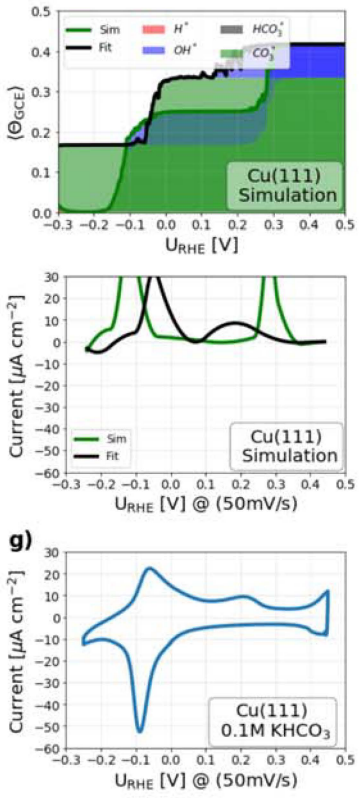

Figure S7: Simulations and fitting of stronger binding CO_3^* coverages for the Cu(111) facet in bicarbonate solution. Fitting parameters are given in Table S9.

Cu(111) KCO_3	E_{fit} [eV]
$E(-1, p, \phi_{e^-})$	0.21
$E(-2, p, \phi_{e^-})$	73.6
$E(-3, p, \phi_{e^-})$	73.7
$E(-4, p, \phi_{e^-})$	73.9
$E(-5, p, \phi_{e^-})$	81.7
$E(-6, p, \phi_{e^-})$	74.1
$E(n = \{1, .., 6\}, p, \phi_{e^-})$	65.7
$E(\{1, 2, 3\}HCO3, p, \phi_{e^-})$	73.5
$E(CO3, p, \phi_{e^-})$	-0.52
$E(2CO3, p, \phi_{e^-})$	-1.19

Table S9: Fitting parameters obtained from fitting AIMD states to experimental $KHCO_3$ CV for Cu(111), when having a stronger binding of CO_3. These values are used in Figure S7.

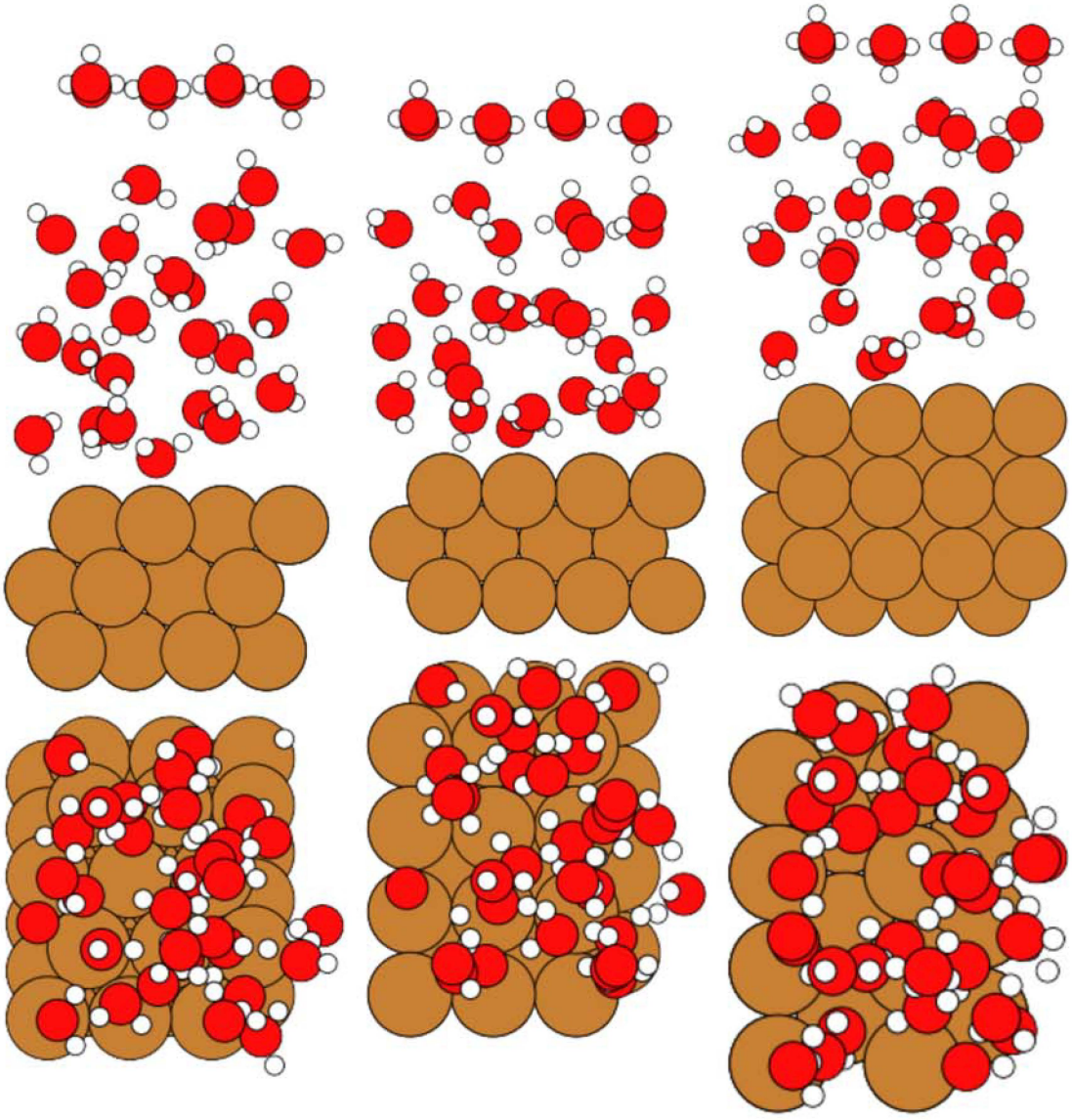

Figure S8: Structural setup of the AIMD simulations. From left the Cu(111), Cu(100) and Cu(110) with sideview and topview, top and bottom, respectively.

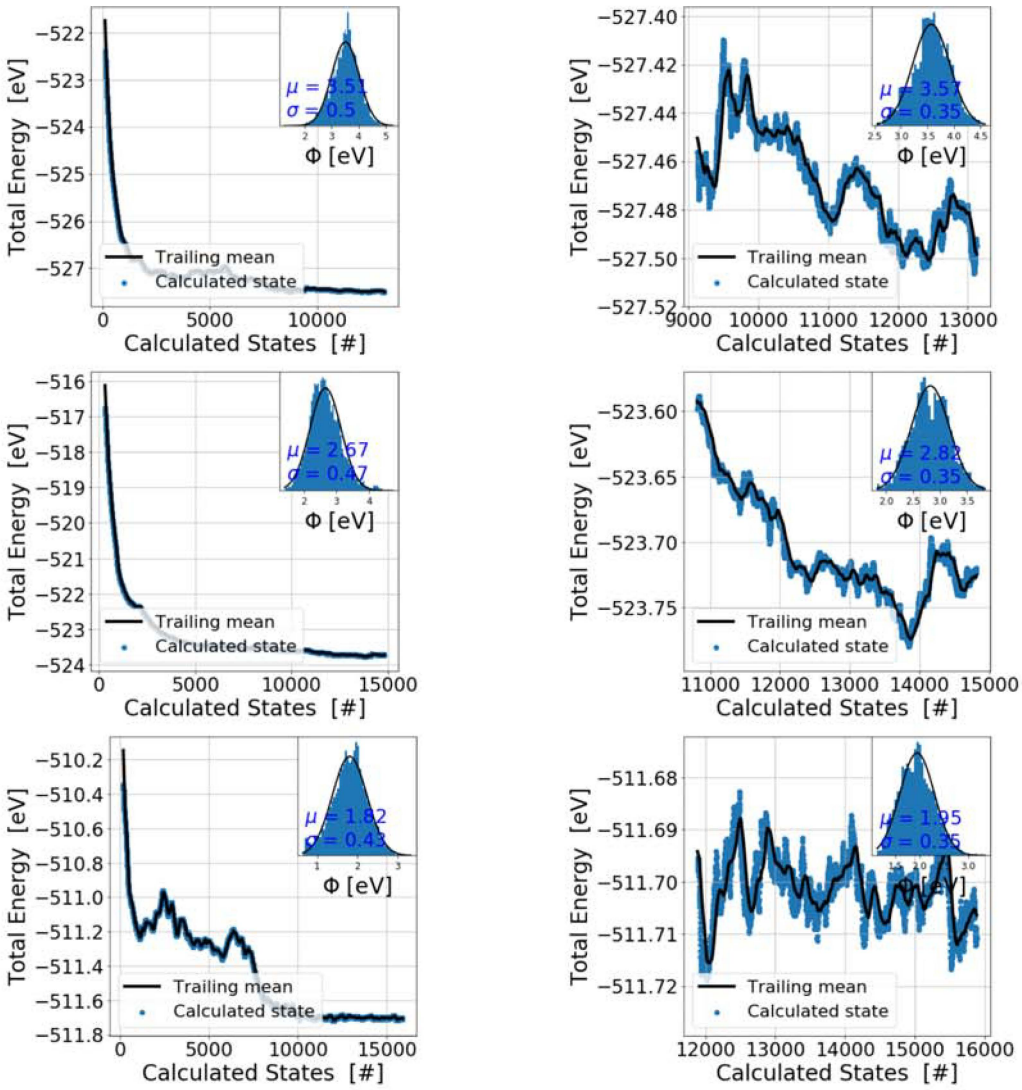

Figure S9: Total energy runs of the AIMD simulations with an insert of the workfunction distribution with a normal fit. Left side full run and right side the last 4000 states. The Cu(111), Cu(100) and Cu(110) is presented in top, middel and bottom row, respectively. Backside workfunction of the setup is found to be 4.14 eV, 3.94 eV, 3.71 eV for Cu(111), Cu(100) and Cu(110), respectively.

References

[1] Atkins, P. and Atkins, P.W. and de Paula, J., *Atkins' Physical Chemistry*, **2014**.

[2] Nørskov, J. K. and Rossmeisl, J. and Logadottir, A. and Lindqvist, L. and Kitchin, J. R. and Bligaard, T. and Jónsson, H., *The Journal of Physical Chemistry B*, **2004**,*108*, 17886-17892